Journal of Power Sources 320 (2016) 204–211

Contents lists available at ScienceDirect

Journal of Power Sources

journal homepage: www.elsevier.com/locate/jpowsour

Realizing full coverage of perovskite film on substrate surface during solution processing: Characterization and elimination of uncovered surface

Yan Li [a], Xue-Long He [b], Bin Ding [a], Li-Li Gao [a], Guan-Jun Yang [a, *], Cheng-Xin Li [a], Chang-Jiu Li [a]

[a] State Key Laboratory for Mechanical Behavior of Materials, School of Materials Science and Engineering, Xi'an Jiaotong University, Xi'an, Shaanxi, 710049, PR China

[b] Jiangxi Province Key Laboratory of Precision Drive and Control, Nanchang, 330099, PR China

HIGHLIGHTS

- The general uncovered areas indeed have an ultra-thin layer of $CH_3NH_3PbI_3$ film.
- Long evaporation time results in localized solute accumulation.
- Localized solute accumulation was responsible for the non-full coverage.
- The full coverage film was achieved by decreasing the solvent evaporation time.
- Perovskite solar cells show η of more than 14% with a full coverage film.

GRAPHICAL ABSTRACT

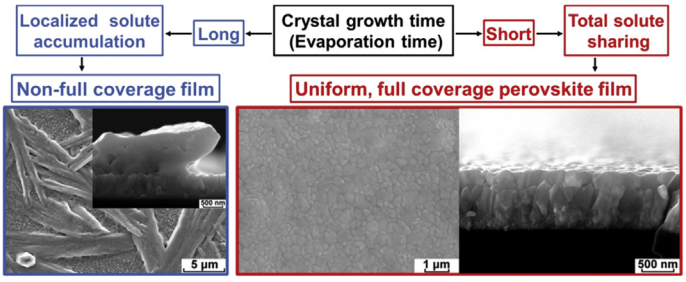

ARTICLE INFO

Article history:
Received 26 January 2016
Received in revised form
18 April 2016
Accepted 20 April 2016
Available online 29 April 2016

Keywords:
$CH_3NH_3PbI_3$ film
Growth behavior
Full coverage
Perovskite solar cells

ABSTRACT

The full coverage of the perovskite film on the substrate surface is of significant importance for the high performance perovskite solar cells. In order to obtain full coverage perovskite films by one-step deposition method, the microstructures of both uncovered areas and covered areas of the $CH_3NH_3PbI_3$ film are comparatively investigated. Results show that the uncovered area indeed has an ultra-thin layer of $CH_3NH_3PbI_3$ film which is too thin to cover the rough surface morphology of the substrate, and the localized solute accumulation due to long crystal growth time is responsible for the non-full coverage of the perovskite film. Then by decreasing the crystal growth time, the localized solute accumulation is eliminated gradually and subsequently a full coverage of perovskite film on substrate surface is realized. As a result, the perovskite solar cells show a conversion efficiency of ~13% with the uniform and full coverage perovskite film.

1. Introduction

Perovskite solar cells are being rapidly developed owing to their low cost, easy fabrication and high photo-to-electric conversion efficiency [1–4]. Recently, the planar heterojunction configuration perovskite solar cells, which are more suitable for roll-to-roll process, have attracted much attention [5–7]. In order to achieve a high efficiency planar solar cell, the perovskite film must be prepared on the substrate with a full coverage to prevent current leakage on the uncovered region [8–11].

* Corresponding author.
E-mail address: ygj@mail.xjtu.edu.cn (G.-J. Yang).

http://dx.doi.org/10.1016/j.jpowsour.2016.04.098
0378-7753/

Until now, one-step deposition method was the most commonly used method to prepare perovskite film due to its low cost and none reverse reaction [12–15]. By using this method, the perovskite films can be simply prepared from precursor solutions containing mixed alkylammonium halides and metal halides by solution film distribution with subsequent natural drying [16–18]. However, the uncontrolled precipitation of perovskite always generates a dendritic structure leaving a lot of uncovered areas on substrate surface [19–21].

Therefore, a couple of methods have been proposed to improve the coverage ratio of the perovskite film by one-step deposition method. Some reports showed that the replacement of inorganic precursor by lead acetate [22] or lead nitrate [23] could improve the film coverage ratio. Besides, adding some additives in the precursor solution, such as hydroiodic acid (HI) [24], 1-chloronaphthalene (CN) [25], poly-(vinylpyrrolidone) (PVP) [26], could also improve the film coverage ratio. However, both types of method need to remove additives, which will bring unpredictable effects to the perovskite film [27,28]. Barrows et al. [29] reported that the coverage ratio was obviously improved with the substrate temperature increased from 28 °C to 75 °C during spray-coating. Jeng et al. [30] found that when the substrate was preheated to 60 °C and the spin-coating speed was improved to 9500 rpm, the number density of void or crevice on the film were markedly reduced. Huang et al. [31] used the 40 psi dry argon gas stream to blow over the film during spin coating, and then a uniform flat $CH_3NH_3PbI_3$ film was formed. According to the above investigations, it was found that the tuning of evaporation, *i.e.* the decrease of the solvent evaporation time, should be beneficial to the full coverage film. However, to the best of our knowledge the relationship between the solvent evaporation time and the microstructures of the films has not been systematically reported, and the fundamental physics from non-full coverage to full coverage is still unclear.

In this study, after a comparatively investigation on the microstructures of both uncovered areas and covered areas of the $CH_3NH_3PbI_3$ films, the formation mechanism of uncovered surface was discussed. By decreasing the crystal growth time, the morphologies evolution of the perovskite films depending on crystal growth time was investigated. Then the full coverage of perovskite film on substrate surface was realized by eliminating the localized solute accumulation. At last, the uniform and full coverage perovskite film was prepared on ZnO/FTO substrate and assembled into planar configuration solar cells.

2. Experimental

2.1. Solution and film preparation

Lead iodide (PbI_2) and methylammonium (ICH_3NH_3) purchased from Weihua Solar Energy Co. (China) were used as solute. *N*, *N*-dimethylformamide (DMF) purchased from Sigma-Aldrich (Germany) was used as solvent. All the chemicals were reagent grade and used without further purification. The transparent fluorine-doped tin oxide (FTO, TEC-15, LOF) conductive glasses (25 mm × 25 mm) were employed as substrates. In addition, the indium-doped tin oxide coated polyethylene naphthalate (ITO-PEN, PECF-IP, Peccell) with a similar rough surface as FTO glass and silicon wafer (Si, IC-Dummy, Branch) were all employed as substrates. Before the film deposition, the substrates were cleaned in successive ultrasonic acetone and alcohol bath followed by drying using high purity nitrogen gas.

For precursor solution preparation, PbI_2 and ICH_3NH_3 with stoichiometric amounts were dissolved in DMF solvents with concentration of 35 wt.% and then kept at 70 °C for more than 5 h by using laboratory type magnetic stirrer. Before perovskite film preparation, the precursor solution was filtered using PTEE filter with a pore size of 0.2 μm. The perovskite film was prepared by the following steps. Firstly, the precursor solution was dropped on the substrate surface and spin-coating at 4000 rpm for 10 s. Secondly, the samples were transferred to a chamber and dried at different low pressures (1800 Pa, 540 Pa, 400 Pa, 170 Pa and 10 Pa). The chamber pressure was controlled automatically by the equipment control unit. All the processes were carried out in air without inert gas protection. During the film preparation the laboratory temperature was kept below 25 °C.

2.2. Device fabrication

A compact layer of ZnO was deposited on the etched FTO substrate (ZnO/FTO substrate) by ion sputtering and then annealed at 120 °C for 15 min. Subsequently, the perovskite film was deposited on the compact ZnO/FTO substrate and dried at the low pressure of 10 Pa. After the as-prepared film was annealed at 100 °C for half an hour, the 2, 2′, 7, 7′ - tetrakis(*N*,*N*-di-*p*-methoxyphenylamine) - 9, 9′ - spirobifluorene (spiro-OMeTAD) based hole transport layer (HTM) was deposited by spin coating at 3000 rpm for 30 s, where the HTM solution consisted of 80 mg spiro-OMeTAD, 28.5 μL 4-tert-butylpyridine and 17.5 μL lithium - bis(trifluoromethanesulfonyl)imide (Li-TFSI) solution (520 mg Li-TFSI in 1 ml acetonitrile), dissolved in 1 ml chlorobenzene. Finally, a 10 nm thick Mo_2O_3 and 200 nm thick Ag layer was deposited on the HTM layer by thermal evaporation respectively.

2.3. Characterization

The surface morphologies of the $CH_3NH_3PbI_3$ films were examined by field emission scanning electron microscopy (FESEM, TESCAN, Czech Republic). The x-ray diffraction (XRD) patterns of perovskite film and substrate were obtained by using an x-ray diffractometer (SHIMADZU, Japan) with Cu Kα radiation. To quantitatively analyze the elements content of the ultra-thin perovskite layer, energy dispersive x-ray spectroscopy (EDS, Oxford, United Kingdom) was employed. The coverage ratio and thickness of the films were calculated with the Image J software (Image J2x, 2011) from the SEM images (at least 10 images for each of data). The photocurrent density-voltage (*J-V*) curves of the solar cells were measured by a solar simulator (84 mW cm^{-2}, Oriel 94023A, Newport) equipped with a Keithley 2400 digital source meter. The exact light intensity was calibrated using a single-crystal silicon photovoltaic cell as the reference (91150V, Oriel Instruments). The cells were measured with a metal mask covered with an area of 0.10 cm^2 to receive sunlight.

3. Results and discussion

3.1. Microstructures of perovskite film prepared by natural drying

Fig. 1a shows the microstructures of the $CH_3NH_3PbI_3$ film prepared by one-step solution method with subsequent natural drying. It can be seen that the perovskite crystals tend to gather together showing a dendritic structure, leaving a large area of nano-rough solid surface. The rough areas (as marked by white triangle in Fig. 1a) are widely recognized to be bare FTO based on the SEM results at a relatively low magnification [13,20,25,30,32]. To make clear that if this kind of rough surface is bare substrate surface, the rough areas was exposed to higher magnification observation. Fig. 1b shows the high magnification surface morphology of this kind of rough surface area. Compared with the surface morphology of a bare FTO substrate in Fig. 1c, it can be seen that, under the natural drying condition, the widely reported

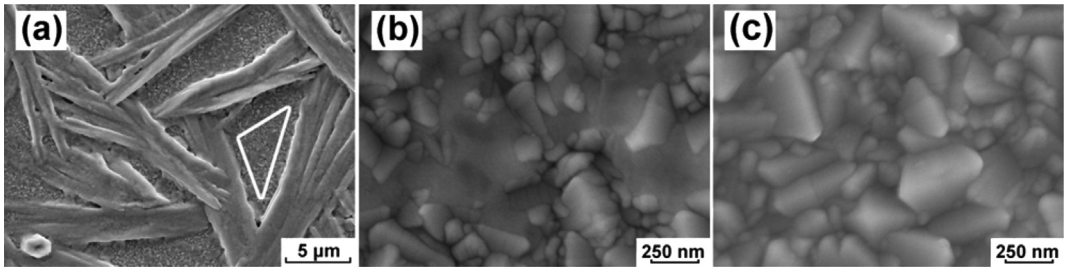

Fig. 1. The surface morphologies of the $CH_3NH_3PbI_3$ film prepared under the natural drying condition (a, b) and the surface morphology of a bare FTO substrate (c). (b) is the high magnification image of the uncovered area in the region with the white triangle mark in (a).

uncovered areas indeed have an ultra-thin layer of film which is too thin to offset the rough surface of the substrate. Only a fraction of this kind of areas is really the bare substrate surface, and the other areas are actually covered with the ultra-thin layer of film. In order to define the nature of these ultra-thin films, similar ultra-thin film area was characterized by EDS. During the characterization process, the working distance of the microscope had to be increased to 15 mm from the initial ~3 mm. As it can be seen in Fig. 2a, through the ultra-thin film showed a little fuzzy morphology because of the long working distance, the roughness of the substrate could also be distinguished. The EDS composition (Fig. 2b inset) results showed that all the objects of the ultra-thin film (objects 1–3) contained the elements of Pb, I, Sn, O and F. Among all of them, Pb and I showed a ratio close to 1:3, which was accordance with the precursor solution of $CH_3NH_3PbI_3$. The different Pb and I contents of every object could be ascribed to the different concave-convex degrees of the bottom substrate. The elements of Sn, O and F may come from the substrate for the exposed FTO substrate (object 4) showing the same signals. Therefore, it can be concluded that under natural drying condition, except for the obvious dendritic $CH_3NH_3PbI_3$ film, there is also an ultra-thin layer of $CH_3NH_3PbI_3$ film in the uncovered area. To our best knowledge, when the coverage ratio of the perovskite film was calculated based on low magnification images (like Fig. 1a similar to most reported literature), only the dendrite morphology perovskite structures was regarded as covering, and the rest of the substrate covered by the ultra-thin layer of perovskite film (as shown in Fig. 1b) was not taken into account. Based on the above results, it should be noted that the conventional coverage ratio only stands for the grown up $CH_3NH_3PbI_3$ film with a dendrite morphology (as shown in Fig. 1a), and thereby the so called coverage ratio in literature up to now refers to an apparent coverage ratio (ACR). It is worth to note that to make clear this definition could be very important to comprehensively understand the formation mechanism of the uncovered area.

To find out what is the reason for the formation of uncovered surface, a sample with both covered and uncovered areas was examined comparatively from both cross section view and plane view (surface morphology) by *in-situ* tilting the sample by 30° within the scanning electron microscope chamber. The results were shown in Fig. 3a–c. The high magnification cross section view of the perovskite film (as shown in Fig. 3c) clearly reveals that the localized film thickness (more than 1 μm for a maximum) is much thicker than the designed thickness which will be illustrated in the next paragraph. Furthermore, even for the dendrite-like perovskite film region, the film also shows a significant non-uniform localized thickness.

The designed thickness is the thickness of an ideal film. Here, the ideal film refers to that the ideally homogeneous film fully covers on the substrate without pin-holes and voids. In order to get the thickness of the ideal film (designed thickness), the weight method was employed. By weight method, the solute weight left on the substrate (25 mm × 25 mm) is 0.62 mg in average after spin-coating at 4000 rpm for 10 s. The density for the bulk $CH_3NH_3PbI_3$ crystal material is 4.159 g cm^{-3} [33]. So the determined $CH_3NH_3PbI_3$ film thickness is 240 nm, *i.e.* designed thickness is 240 nm. Based on the average (or designed) film thickness, the localized film thickness can be compared and further discussed to aim at comprehensively understanding the formation mechanism of non-uniform film thickness.

To further quantitatively evaluate the thickness distribution, many images like Fig. 3a were subjected to a statistical observation. Fig. 3d shows the distribution of the localized perovskite film thickness. The zero thickness refers to the rough surface with an ultra-thin layer of perovskite film. It can be found that the localized film thickness is broadly distributed in a range from 0 to 2000 nm, and most of the localized film thickness significantly deviates from the designed thickness (240 nm in this case).

Generally, the crystallization process in solution is composed of supersaturation, nucleation and growth. The crystals come into growth step immediately after the stable nuclei appear in solution. In addition, the growth step does not finish until the solution is completely exhausted during the solvent evaporation process.

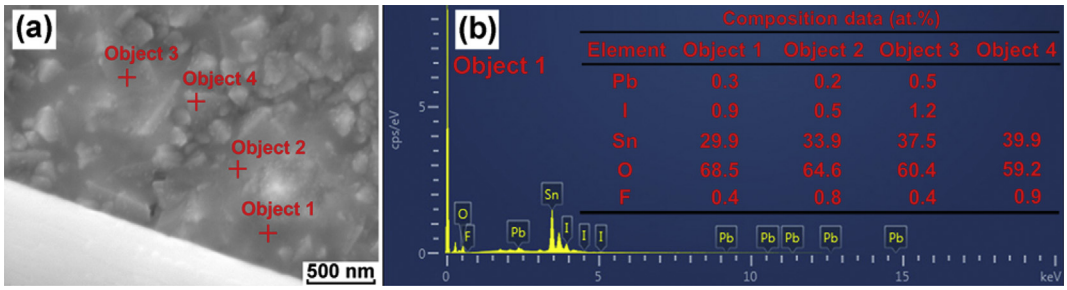

Fig. 2. The surface morphology of the ultra-thin $CH_3NH_3PbI_3$ film detected under working distance of 15 mm (a) and the EDS spectrum of object 1 (b). The (b) inset shows the corresponding EDS composition data of objects 1–4 signed in (a).

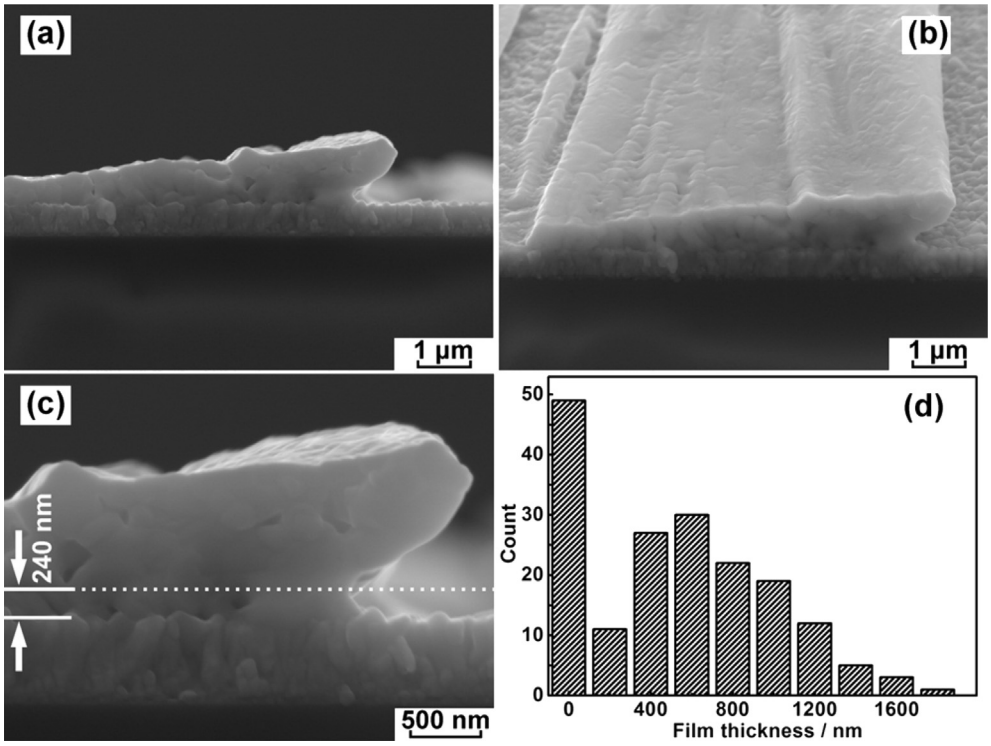

Fig. 3. The cross sections of the $CH_3NH_3PbI_3$ film prepared under the natural drying condition (a–c), and the film thickness distribution (d).

Based on the above results, it is obvious that, under natural drying condition, the solvent evaporation time is long enough for the original crystals to have enough time to grow up even significantly exceeding the designed thickness (240 nm). In short, the overgrowth phenomenon leads to the localized solute accumulation. Definitely, the superabundant of the precursor in localized areas will make the residual areas have no enough feedstock to grow to a mean thickness. As a result, a thin layer of $CH_3NH_3PbI_3$ film has to be formed on the substrate surface as shown in Fig. 1b and Fig. 2a. Therefore, it can be concluded that, under natural drying condition, the serious localized solute accumulation for long solvent evaporation time (crystal growth time) should be responsible for the non-full coverage of the perovskite film.

3.2. Evolution of film microstructures by tuning evaporation process

In order to enhance the solvent evaporation, *i.e.* to decrease the crystal growth time, a low pressure drying method was employed. During the low pressure drying process, the solvent evaporation rate increases with decreasing chamber pressure, and thereby the solvent evaporation time (crystal growth time) is decreased with decreasing the chamber pressure.

Fig. 4 shows the surface morphologies of the $CH_3NH_3PbI_3$ perovskite films with decreasing the solvent evaporation time (crystal growth time). When the low pressure was decreased to 1800 Pa as shown in Fig. 4a–c, the perovskite crystals still tended to gather together showing a dendritic structure leaving a large area of nano-rough solid surface. This was similar to the film prepared at natural drying condition in Fig. 1a. With further decreasing evaporation time (decreasing low pressure to 540 Pa) as shown in Fig. 4d–f, the surface of the film seemed still to maintain a dendritic structure leaving a lot of in-continuous small uncovered areas. However, compared with Fig. 4a–c, the size of the dendritic structure in Fig. 4d–f was much smaller and showed a dispersion state. With further decreasing evaporation time (further decreasing low pressure to 400 Pa) as shown in Fig. 4g–i, the dendritic structure almost disappeared, and the perovskite crystals were well connected to each other on the substrate. However, there were still some uncovered areas randomly distributed on the substrate. When the low pressure went on being decreased to 170 Pa as shown in Fig. 4j–l, the film showed a relatively rough surface morphology. Moreover, the dendritic structure and the uncovered area almost disappeared. At last when the low pressure reached to 10 Pa, an extremely uniform and flat film was received as shown in Fig. 4m–o. It shows no any pinhole and uncovered area on the whole sample surface. Furthermore, it can also be found that the perovskite grain size from the plane view also decreases with decreasing evaporation time from Fig. 4c–o.

To quantitatively evaluate the perovskite film coverage on substrate surface, the film ACR (defined in the section 3.1) was statistically analyzed using images like Fig. 4a,d,g,j,m and listed as the insets in those figures. The accurate data of ACR show that the coverage ratio is increased with decreasing of the solvent evaporation time (crystal growth time). When the pressure decreased to 10 Pa, a 100.0% apparent coverage ratio, indicating a full coverage $CH_3NH_3PbI_3$ film on substrate surface, had been realized.

To further classify the elimination of uncovered substrate surface, the cross sections of the $CH_3NH_3PbI_3$ films were comparatively observed as shown in Fig. 5. It can be seen that the localized film thickness tends to decrease with decreasing solvent evaporation time, and finally an extremely uniform film thickness is realized for Fig. 5m. In addition, the film becomes flatter with decreasing solvent evaporation time. Furthermore, it can be found that the perovskite grain size from the plane view also decreases with decreasing evaporation time from Fig. 5b–n, which is consistent with the results in Fig. 4c–o. In order to obtain an accurate result, the statistical analysis of localized film thickness and grain size was performed as shown in Fig. 5c–o. It can be seen from film thickness bar graph that when the solvent evaporation time is long, such as

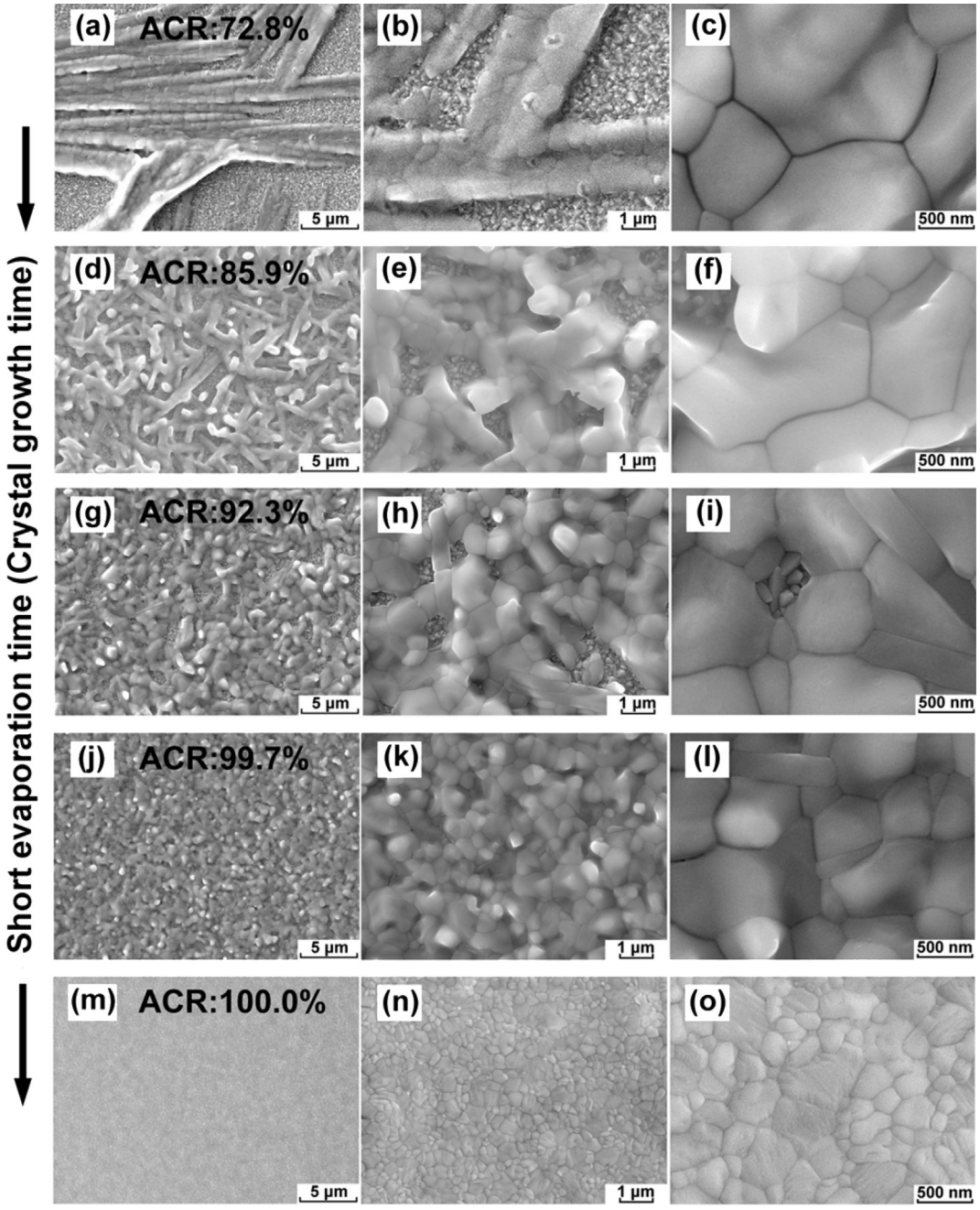

Fig. 4. The surface morphologies of the $CH_3NH_3PbI_3$ perovskite films drying with decreasing solvent evaporation time (crystal growth time): 1800 Pa (a–c); 540 Pa (d–f); 400 Pa (g–i); 170 Pa (j–l); 10 Pa (m–o).

the result shown in Fig. 5c, the film thickness is widely distributed from 0 nm to 1600 nm. Whereas, when the solvent evaporation time is short, such as the result shown in Fig. 5o, the film thickness tends to centralized to 240 nm, and the film thickness is only distributed in a range from 210 nm to 270 nm, which is comparable to the designed thickness (240 nm).

Besides, the grain size (from plan view as shown in Fig. 4) of the film prepared with decreasing solvent evaporation time was also investigated. It can be seen from the grain size bar graph in Fig. 5 that the grain size is also decreased with decreasing solvent evaporation time. At a low pressure of 10 Pa, the average grain size of the $CH_3NH_3PbI_3$ film is decreased to ~300 nm, while it is still larger than the previous results [5,34,35]. Though the large grain size is useful for a long charge lifetime and reduced trap density [36], Im et al. [37] illustrated that the optimal grain size of ~300 nm for the perovskite film presented the best photovoltaic performance.

3.3. Photovoltaic performance of the perovskite solar cells with a uniform and full coverage $CH_3NH_3PbI_3$ film

Based on the above results, it can be seen that, under natural drying condition, the long evaporation time (crystal growth time) leads to localized solute accumulation which results in the over-growth of the perovskite crystals. Finally the non-full coverage perovskite film is prepared. Therefore, by decreasing solvent

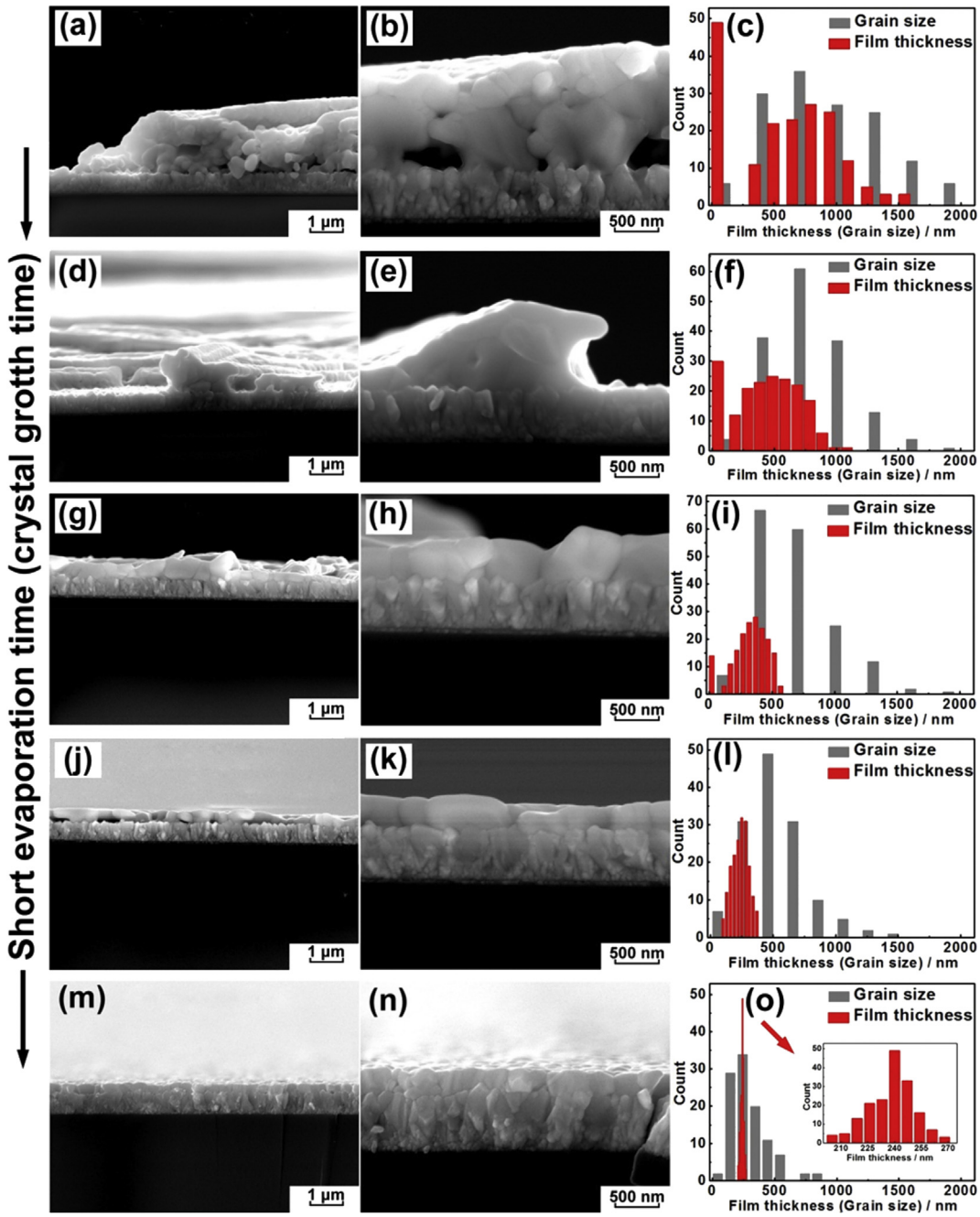

Fig. 5. The cross sections of the $CH_3NH_3PbI_3$ perovskite films drying with decreasing solvent evaporation time (crystal growth time): 1800 Pa (a–b); 540 Pa (d–e); 400 Pa (g–h); 170 Pa (j–k) and 10 Pa (m–n). The film thickness distribution (red bar graph) and the grain size distribution (gray bar graph) with decreasing solvent evaporation time (crystal growth time): 1800 Pa (c), 540 Pa (f), 400 Pa (i), 170 Pa (l) and 10 Pa (n). ACR stands for the apparent coverage ratio of perovskite film on substrate surface. (For interpretation of the references to colour in this figure legend, the reader is referred to the web version of this article.)

evaporation time (crystal growth time), the overgrowth phenomenon of the perovskite film is restrained. The uniform and full coverage perovskite films are realized on the bare FTO substrates at last. Then by decreasing crystal growth time at a pressure of 10 Pa, the uniform and full coverage perovskite films were also prepared on the other types of substrates, such as ZnO/FTO substrate (Fig. 6a), ITO-PEN substrate (Fig. S1a) and silicon wafer substrate (Fig. S1b).

As shown in Fig. 6a, the perovskite film still shows a uniform and full coverage state on the ZnO/FTO substrate. Before the assembling of the solar cell devices, the crystalline structure of the perovskite film was firstly examined by x-ray diffraction analysis. Fig. 6b shows that the XRD spectra of the perovskite films deposited on the ZnO/FTO substrate, FTO substrate and the XRD spectrum of a bare FTO substrate. The main diffraction peaks in both $CH_3NH_3PbI_3$/ZnO/FTO pattern and $CH_3NH_3PbI_3$/FTO pattern are assigned to the tetragonal perovskite (110), (220) and (310), respectively, indicating a high level of phase purity [38]. There is no ZnO diffraction peak in $CH_3NH_3PbI_3$/ZnO/FTO pattern, which may be ascribed to the low annealing temperature (120 °C) inducing no crystallization of ZnO compact layer. Then perovskite solar cell devices were assembled and tested under simulated sunlight irradiation. The perovskite solar cells were fabricated into the common planar architecture as

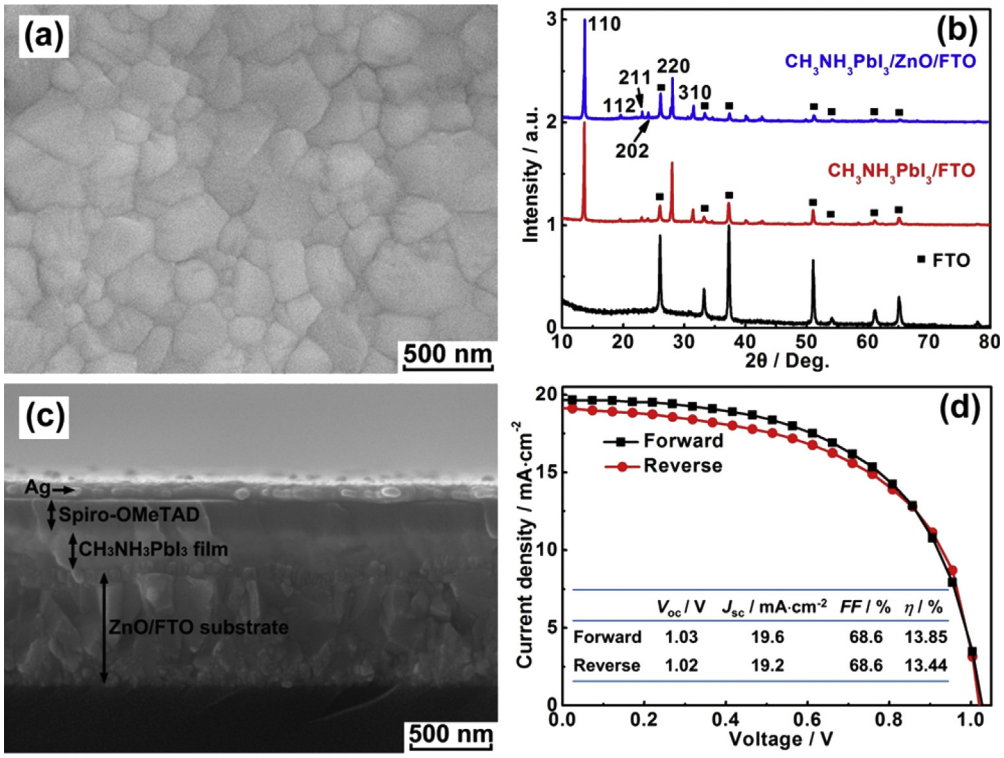

Fig. 6. The surface morphology of the $CH_3NH_3PbI_3$ film prepared under low pressure of 10 Pa on the ZnO/FTO substrate (a). The XRD spectra of the perovskite films deposited on the ZnO/FTO substrate, FTO substrate and the XRD spectrum of a bare FTO substrate (b). The cross section view of the planar configuration perovskite solar cell with the device architecture of FTO/ZnO compact layer/$CH_3NH_3PbI_3$/Spiro-OMeTAD/Mo_3O_2/Ag (c). The photocurrent density-voltage (*J*–*V*) curves of the perovskite solar cells at forward and reverse scans, respectively (d).

shown in Fig. 6c (FTO/ZnO compact layer/$CH_3NH_3PbI_3$/Spiro-OMeTAD/Mo_2O_3/Ag). One of the corresponding photocurrent density-voltage (*J-V*) curves is shown in Fig. 6d. It can be seen that the hysteresis is not obvious. The open circuit voltage (V_{oc}) is more than 1 V, while the short circuit current (J_{sc}) is about 19 mA cm^{-2}. At last, the conversion efficiency is more than 13%, and the inset further lists detailed photovoltaic parameters. In addition, more detailed *J-V* curves of the solar cells were shown in Fig. S2. The result reveals that the uniform and full coverage film prepared by decreasing crystal growth time shows a fairly good performance.

4. Conclusion

In this study, by comparatively characterizing the microstructures of $CH_3NH_3PbI_3$ films drying under both natural condition and the low pressure evaporation, the formation mechanism of uncovered surface was investigated. It was found that the uncovered areas indeed had an ultra-thin layer of $CH_3NH_3PbI_3$ film, and the serious localized solute accumulation for long solvent evaporation time (crystal growth time) was responsible for the non-full coverage of the perovskite films. Moreover, by decreasing the solvent evaporation time (crystal growth time), the apparent coverage ratio was increased. Besides, the film thickness became more and more uniform by decreasing the solvent evaporation time (crystal growth time). Furthermore, through tuning the evaporation time, the flat and full coverage perovskite film with the average thickness of 240 nm was realized on many types of substrates at last. The assembled perovskite solar cells showed the conversion efficiency of ~13% by using this uniform and full coverage perovskite film.

Acknowledgements

The work was supported by the National Program for Support of Top-notch Young Professionals.

Appendix A. Supplementary data

Supplementary data related to this article can be found at http://dx.doi.org/10.1016/j.jpowsour.2016.04.098.

References

[1] N.G. Park, J. Phys. Chem. Lett. 4 (2013) 2423–2429.
[2] K.Y. Yan, M.Z. Long, T.K. Zhang, Z.H. Wei, H.N. Chen, S.H. Yang, J.B. Xu, J. Am. Chem. Soc. 137 (2015) 4460–4468.
[3] C.G. Wu, C.H. Chiang, Z.L. Tseng, M.K. Nazeeruddin, A. Hagfeldt, M. Gratzel, Energy Environ. Sci. 8 (2015) 2725–2733.
[4] F. Di Giacomo, S. Razza, F. Matteocci, A. D'Epifanio, S. Licoccia, T.M. Brown, A. Di Carlo, J. Power Sources 251 (2014) 152–156.
[5] J.W. Jung, S.T. Williams, A.K.Y. Jen, Rsc Adv. 4 (2014) 62971–62977.
[6] P. Docampo, J.M. Ball, M. Darwich, G.E. Eperon, H.J. Snaith, Nat. Commun. 4 (2013) 3761.
[7] Y. Dkhissi, F. Huang, S. Rubanov, M. Xiao, U. Bach, L. Spiccia, R.A. Caruso, Y.B. Cheng, J. Power Sources 278 (2015) 325–331.
[8] J. Liu, J. Lin, Q. Xue, Q. Ye, X. He, L. Ouyang, D. Zhuang, C. Liao, H.L. Yip, J. Mei, W.-M. Lau, J. Power Sources 301 (2016) 242–250.
[9] L.K. Huang, Z.Y. Hu, G.Q. Yue, J.W. Liu, X.H. Cui, J. Zhang, Y.J. Zhu, Phys. Chem. Chem. Phys. 17 (2015) 22015–22022.
[10] F.X. Xie, D. Zhang, H.M. Su, X.G. Ren, K.S. Wong, M. Gratzel, W.C.H. Choy, Acs Nano 9 (2015) 639–646.
[11] H. Deng, D. Dong, K. Qiao, L. Bu, B. Li, D. Yang, H.-E. Wang, Y. Cheng, Z. Zhao, J. Tang, H. Song, Nanoscale 7 (2015) 4163–4170.
[12] H.S. Kim, C.R. Lee, J.H. Im, K.B. Lee, T. Moehl, A. Marchioro, S.J. Moon, R. Humphry-Baker, J.H. Yum, J.E. Moser, M. Gratzel, N.G. Park, Sci. Rep. UK 2 (2012) 591.
[13] G.E. Eperon, V.M. Burlakov, P. Docampo, A. Goriely, H.J. Snaith, Adv. Funct. Mater. 24 (2014) 151–157.

[14] Z.L. Ku, Y.G. Rong, M. Xu, T.F. Liu, H.W. Han, Sci. Rep. UK 3 (2013) 3132.
[15] B. Conings, L. Baeten, C. De Dobbelaere, J. D'Haen, J. Manca, H.G. Boyen, Adv. Mater. 26 (2014) 2041–2046.
[16] J.H. Im, C.R. Lee, J.W. Lee, S.W. Park, N.G. Park, Nanoscale 3 (2011) 4088–4093.
[17] A. Kojima, K. Teshima, Y. Shirai, T. Miyasaka, J. Am. Chem. Soc. 131 (2009) 6050–6051.
[18] Y. Zhang, W. Liu, F. Tan, Y. Gu, J. Power Sources 274 (2015) 1224–1230.
[19] C.C. Chueh, C.Y. Liao, F. Zuo, S.T. Williams, P.W. Liang, A.K.Y. Jen, J. Mater. Chem. A 3 (2015) 9058–9062.
[20] L.J. Zuo, Z.W. Gu, T. Ye, W.F. Fu, G. Wu, H.Y. Li, H.Z. Chen, J. Am. Chem. Soc. 137 (2015) 2674–2679.
[21] T. Salim, S.Y. Sun, Y. Abe, A. Krishna, A.C. Grimsdale, Y.M. Lam, J. Mater. Chem. A 3 (2015) 8943–8969.
[22] W. Zhang, M. Saliba, D.T. Moore, S.K. Pathak, M.T. Horantner, T. Stergiopoulos, S.D. Stranks, G.E. Eperon, J.A. Alexander-Webber, A. Abate, A. Sadhanala, S.H. Yao, Y.L. Chen, R.H. Friend, L.A. Estroff, U. Wiesner, H.J. Snaith, Nat. Commun. 6 (2015) 6142.
[23] T.Y. Hsieh, T.C. Wei, K.L. Wu, M. Ikegami, T. Miyasaka, Chem. Commun. 51 (2015) 13294–13297.
[24] G.E. Eperon, S.D. Stranks, C. Menelaou, M.B. Johnston, L.M. Herz, H.J. Snaith, Energ. Environ. Sci. 7 (2014) 982–988.
[25] X. Song, W.W. Wang, P. Sun, W.L. Ma, Z.K. Chen, Appl. Phys. Lett. 106 (2015) 033901.
[26] Y.L. Ding, X. Yao, X.D. Zhang, C.C. Wei, Y. Zhao, J. Power Sources 272 (2014) 351–355.
[27] S.D. Stranks, P.K. Nayak, W. Zhang, T. Stergiopoulos, H.J. Snaith, Angew. Chem. Int. Ed. 54 (2015) 3240–3248.
[28] K.W. Tan, D.T. Moore, M. Saliba, H. Sai, L.A. Estroff, T. Hanrath, H.J. Snaith, U. Wiesner, Acs Nano 8 (2014) 4730–4739.
[29] A.T. Barrows, A.J. Pearson, C.K. Kwak, A.D.F. Dunbar, A.R. Buckley, D.G. Lidzey, Energ. Environ. Sci. 7 (2014) 2944–2950.
[30] J.Y. Jeng, K.C. Chen, T.Y. Chiang, P.Y. Lin, T.D. Tsai, Y.C. Chang, T.F. Guo, P. Chen, T.C. Wen, Y.J. Hsu, Adv. Mater. 26 (2014) 4107–4113.
[31] F.Z. Huang, Y. Dkhissi, W.C. Huang, M.D. Xiao, I. Benesperi, S. Rubanov, Y. Zhu, X.F. Lin, L.C. Jiang, Y.C. Zhou, A. Gray-Weale, J. Etheridge, C.R. McNeill, R.A. Caruso, U. Bach, L. Spiccia, Y.B. Cheng, Nano Energy 10 (2014) 10–18.
[32] C.Y. Chang, C.Y. Chu, Y.C. Huang, C.W. Huang, S.Y. Chang, C.A. Chen, C.Y. Chao, W.F. Su, Acs Appl. Mater. Interfaces 7 (2015) 4955–4961.
[33] C.C. Stoumpos, C.D. Malliakas, M.G. Kanatzidis, Inorg. Chem. 52 (2013) 9019–9038.
[34] Z.G. Xiao, Q.F. Dong, C. Bi, Y.C. Shao, Y.B. Yuan, J.S. Huang, Adv. Mater. 26 (2014) 6503–6509.
[35] A. Listorti, E.J. Juarez-Perez, C. Frontera, V. Roiati, L. Garcia-Andrade, S. Colella, A. Rizzo, P. Ortiz, I. Mora-Sero, J. Phys. Chem. Lett. 6 (2015) 1628–1637.
[36] D. Shi, V. Adinolfi, R. Comin, M.J. Yuan, E. Alarousu, A. Buin, Y. Chen, S. Hoogland, A. Rothenberger, K. Katsiev, Y. Losovyj, X. Zhang, P.A. Dowben, O.F. Mohammed, E.H. Sargent, O.M. Bakr, Science 347 (2015) 519–522.
[37] T. Baikie, Y.N. Fang, J.M. Kadro, M. Schreyer, F.X. Wei, S.G. Mhaisalkar, M. Graetzel, T.J. White, J. Mater. Chem. A 1 (2013) 5628–5641.
[38] J.H. Im, I.H. Jang, N. Pellet, M. Gratzel, N.G. Park, Nat. Nanotechnol. 9 (2014) 927–932.